석사학위논문

독립 제어 가능 마이크로파 이중 대역 가변 위상 변환기

2024년 2월 22일

전 북 대 학 교 대 학 원

전 자 정 보 공 학 부

Samdy Saron

독립 제어 가능 마이크로파 이중 대역 가변 위상 변환기

Dual-Band Microwave Variable Phase Shifter With Individual Controls

2024년 2월 22일

전 북 대 학 교 대 학 원

전 자 정 보 공 학 부

Samdy Saron

독립 제어 가능 마이크로파 이중 대역 가변 위상 변환기

지도교수 정용채

이 논문을 공학 석사 학위논문으로 제출함.

2023년 10월 18일

전 북 대 학 교 대 학 원

전 자 정 보 공 학 부

Samdy Saron

Samdy Saron 의 석사학위논문을 인준함.

위 원 장	전북대학교	교 수	손해원	(인)
부위원장	전북대학교	교 수	임동구	(인)
위 원	전북대학교	교 수	정용채	(인)

2024년 1월 8일

전 북 대 학 교 대 학 원

Contents

List of Figures

List of Acronyms

CL1	Coupled line at lower band circuit
CL2	Coupled line at higher band circuit
C_V	Varactor diode
DPS	Dual-band phase shifter
ITPS	Independent tunable phase shifter
PDE	Phase diviation error
PSR	Phase shift range
MMIC	Concurrent dual-band monolithic microwave integrated circuit
TL	Transmsion line

ABSTRACT

Dual-Band Microwave Variable Phase Shifter with Individual Controls

Samdy Saron
Division of Electronics Engineering
The Graduate School
Jeonbuk National University

This dissertation presents a design of reflection-type dual-band phase shifter (PSR) which allows to tune relative phase shift at two operating frequency bands independently. The proposed phase shifter consists of a 3-dB hybrid coupler where through and couple ports are terminated with reflection loads. Each reflection load comprises of couple line (CL), a transmission line (TL) and a varactor diode. The CL can achieve independent phase tuning at each operating frequency, while TL terminated with varactor diode is used to high relative PSR. To prove the validity of the proposed method, the dual-band phase shifter operating at center frequencies of 1.88 GHz and 2.44 GHz is designed and fabricated. The measured relative PSR is 149.33° at 1.88 GHz with phase derivation error (PDE) of ±8.45° within 300 MHz bandwidth. Similarly, the PSR at 2.44 GHz is 125.25° with PDE of ±8.36° within 300 MHz bandwidth. Likewise, the minimum return loss of around 17.36 dB, and the maximum insertion loss of 1.81 dB are measured at both operating bands.

Keywords: Coupled line, dual-band tunable phase shifter independent phase control, varactor diode.

Chapter 1 Introduction

A tunable phase shifter typically modifies the phase of an input signal by changing the electrical path length or the propagation velocity of the signal within the device. This is often achieved using variable reactance components like varactor diodes or using mechanical means in some cases.

The tuning or control of the phase shift can be achieved through various methods. In electronic tunable phase shifters, this is often done by varying the voltage applied to a reactive component like a varactor diode, which changes its capacitance and thus alters the phase shift. Other methods might include mechanical adjustment of the phase shifter physical structure or using magnetic or ferroelectric materials whose properties can be changed with an external magnetic field or electric field.

Tunable phase shifter is used to control a phase of a signal which has been found wide range of various applications including beamforming [1], phased array antenna [2], self-interference cancellation [3]. To support multi-band wireless communications, it is necessary to design tunable phase shifter that operates over multiple frequency bands simultaneously. However, previously reported tunable phase shifters are mainly designed for single frequency band operations, which fail to provide independently controllable transmission phase shift over multi-band frequency operation. [4], [5], [6], [7].

Recently, a dual-band 90-degree SiGe HBT active phase shifter is presented in [8] using bandpass and bandstop filters in load circuit. In [9], dual-band phase shifter (DPS) is designed by using two stub-loaded transmission lines (TLs) and two delay lines. Similarly, dual-band differential phase shifter is presented in [10] that utilized slope alignment of coupled line resonators.

However, these DPSs cannot provide independent tunable phase shift (ITPS) at two operating bands. Concurrent dual-band monolithic microwave integrated circuit (MMIC) tunable phase shifter is reported in [11] utilizing two-stage dual-branch phase tuning network topology. A reflection-type DPS with ITPS is presented in [12] using λ/4 series and shunt TLs. However, this work requires compensation shunt elements at each operating band to compensate parasitic effect of λ/4 shunt TL for achieving ITPS and high relative phase shift tuning range (PSR).

In this work, reflection-type dual-band tunable phase shifter is proposed using coupled lines terminated with TLs and varactor diodes, which does not require any compensation elements. The coupled lines have been utilized for achieving independent phase control at each operating band as well as improving PSR. The proposed DPS can provide independent tunable phase at each operating band as well as simultaneous tunable phase shift at both bands.

Chapter 2 3-dB Hybrid Coupler

In the field of RF engineering, a reflective phase shifter typically comprises a 90° hybrid coupler combined with reflection loads. This setup is designed such that when an input is applied to port 1 of the hybrid coupler, it ensures an equal power distribution (3 dB) to the output port 3 and 4. A notable characteristic of this system is that the outputs at these ports have a 90° phase difference. When identical reflection loads, possessing only reactance, are connected to these output ports, they exploit the phase shifts resulting from the reflections load. This configuration is adept at adjusting the phase between port 1 and 2 while keeping the signal amplitude changes to a minimum. The phase shift range between these ports is effectively the same as that of a single reflection load. This phenomenon and its implications are validated through the port reduction method, a technique that derives the scattering matrix of a network by reducing the number of active ports. Interestingly, this method reveals that in this setup, the reflected signals at port 1 from both loads exhibit a 180° phase difference, effectively cancelling each other out and leading to superior reflection loss characteristics. The reverse application of this method is utilized to deduce the two-port scattering matrix of the reflective phase shifter from the four-port 90° hybrid coupler, thus enabling a detailed analysis of its phase characteristics. This approach underlines the efficiency and precision of the reflective phase shifter in managing phase shifts, crucial for various applications in RF system. Fig.2.1. shows the structure of reflection-type tunable phase shifter.

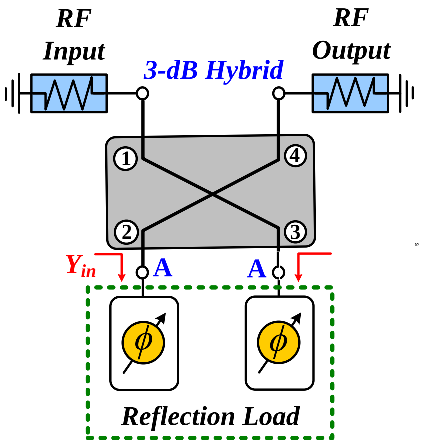

Fig. 2.1. Structure of reflection-type tunable phase shift

The scattering matrix of four-port networks can be expressed in equation 2.1.

$$S_{\text{4-ports}} = \begin{bmatrix} 0 & 0 & -1 & j \\ 0 & 0 & j & -1 \\ -1 & j & 0 & 0 \\ j & -1 & 0 & 0 \end{bmatrix} \tag{2.1}$$

This four-port circuit can be considered as divided into two parts: ports 1 to 2 and ports 3 to 4. This network is conceptually divided into two distinct sections: one comprising ports 1 and 2, and the other encompassing ports 3 and 4. Such a division allows for a more manageable analysis of the circuit's characteristics. In this scenario, the S-parameters, which are crucial for understanding how RF signals behave within the network, are expressed separately for each two-port section. These parameters, likely detailed in equation (2.2), are instrumental in determining how much signal is transmitted, reflected, or lost in each part of the circuit.

$$S_{11} = \begin{bmatrix} 0 & 0 \\ 0 & 0 \end{bmatrix}, S_{21} = -\frac{1}{\sqrt{2}}\begin{bmatrix} -1 & j \\ j & -1 \end{bmatrix}, S_{12} = -\frac{1}{\sqrt{2}}\begin{bmatrix} -1 & j \\ j & -1 \end{bmatrix}, S_{22} = \begin{bmatrix} 0 & 0 \\ 0 & 0 \end{bmatrix} \tag{2.2}$$

Additionally, the determinant of the *S*-parameter matrix, referenced as equation (2.3), plays a significant role in providing insights into the overall behavior of the network. The terms 'a' and 'b' are used to denote the incident and reflected waves, respectively.

$$\begin{aligned} b_1 &= S_{11}a_1 + S_{12}a_2 \\ b_2 &= S_{21}a_1 + S_{22}a_2 \end{aligned} \tag{2.3}$$

Let's consider a two-port circuit with reflection loads terminated to ports 3 and 4, having the same input admittance Y_{in}. If the reflection coefficient at ports 3 and 4 is denoted as Γ_{in}, then the *S*-parameter matrix and its determinant for the reflection load are as given in equations (2.4) and (2.5), respectively.

$$S_{in} = \begin{bmatrix} \Gamma_{in} & 0 \\ 0 & \Gamma_{in} \end{bmatrix} \tag{2.4}$$

$$b' = S_{in}a' \tag{2.5}$$

From the relationship between the incident and reflected waves between the connected coupler and the reflective load, the following equation can be derived.

$$a_2 = S_{in}b_2 \tag{2.6}$$

By substituting the relationship of Equation (2.6) into Equation (2.3) and using this to rearrange Equation (2.3) in terms of a_1 and b_1, we obtained the following.

$$\begin{aligned} b_1 &= S_{11}a_1 + S_{12}a_2 \\ b_2 &= S_{21}a_1 + S_{22}a_2 \end{aligned} \tag{2.7}$$

$$\frac{b_1}{a_1} = S_{11} + S_{12} S_{in} \left(U - S_{22} S_{in} \right)^{-1} S_{21} \tag{2.8}$$

By substituting Equations (2.4) and (2.2) for the parameters corresponding to Equation (2.8), the *S*-parameter matrix of the new two-port network with the reflection load can be obtained as Equation (2.9).

$$S_{2-port} = \begin{bmatrix} 0 & -j\Gamma_{in} \\ -j\Gamma_{in} & 0 \end{bmatrix} \tag{2.9}$$

The reflection coefficient Γ_{in} of the reflection load, the phase shift (ϕ), and the maximum phase shift range ($\Delta\phi$), are presented in Equation (2.10).

$$\begin{aligned} \Gamma_{in} &= \frac{jY_{in} - Y_0}{jY_{in} + Y_0} \\ \phi_{in} &= \pi - \tan^{-1}\left(\frac{Y_{in}}{Y_0} \right) - \tan^{-1}\left(\frac{Y_{in}}{Y_0} \right) = \pi - 2\tan^{-1}\left(\frac{Y_{in}}{Y_0} \right) \\ \Delta\phi_{in} &= \phi_{in}\big|_{\max} - \phi_{in}\big|_{\min} \end{aligned} \tag{2.10}$$

where $Y_0 = 1/Z_0$ is a port termination admittance. Y_{in} is the total input admittance of the reflection load in the note A of Fig. 2.1.

As can be seen from equations (2.10), it is apparent that the overall phase shift range ($\Delta\phi$) of the reflection load. Therefore, by designing the reflection load, the desired phase shift range characteristic of the entire phase shifter can be obtained. If the reflection load only has a capacitive component in its reactance, it can be considered to be determined by the frequency (f) and the variable capacitance C_V of the varactor diode. Consequently, the phase shift (ϕ)can be represented as a function of f and C_V.

$$\phi_{in}\left(f, C_V \right) = \pi - 2\tan^{-1}\left(\frac{Y_{in}}{Y_0}\left(f, C_V \right) \right) \tag{2.11}$$

From equation (2.11), the phase shift range at the operating frequency due to the variation of the variable capacitance C_V from its minimum capacitance $C_{V\_\min}$ to its maximum capacitance $C_{V\_\max}$ can be calculated as shown in equation (2.12).

$$\Delta\phi(C_V)\big|_{f_c} = \phi(C_V)\big|_{f_c} - \phi(C_V)_{\min}\big|_{f_c} \text{ , when } \phi(C_V)_{\min}\big|_{f_c} < \phi(C_V)_{\max}\big|_{f_c} \tag{2.12a}$$

$$\Delta\phi(C_V)\big|_{f_c} = \phi(C_V)\big|_{f_c} - \phi(C_V)_{\max}\big|_{f_c} \text{ , when } \phi(C_V)_{\max}\big|_{f_c} < \phi(C_V)_{\min}\big|_{f_c} \tag{2.12b}$$

Additionally, in-band phase deviation error (PDE) within the operating bandwidth can be expressed as shown in equation (2.13).

$$\mathrm{PDE}(C_V) = \frac{\max\left(\Delta\phi(C_V)\right)\big|_{BW} - \min\left(\Delta\phi(C_V)\right)\big|_{BW}}{2} \tag{2.13}$$

3.1. Reflection load

Fig. 3.1 shows the reflection load which consists of coupled lines terminated TL and varactor diode operating at lower and higher band frequencies. The tunable phase operation at high or low band can affect to other low or high band, and these interferences must be prevented to achieve independent phase shift at each operating band. Therefore, it is necessary to cancel the interference effect so that the proposed DPS can provide independent tunable phase at each operating band as well as simultaneous tunable phase shift at both bands operation. For the purpose of achieving independent phase control at each band, coupled lines are used. The total input admittance looking at point A in Fig. 3.1 is given as (1) where f, f_L, and f_H are operating frequency, lower band center frequency, and higher band center frequency, respectively.

$$Y_{in} = Y_{inL} + Y_{inH} \tag{3.1}$$

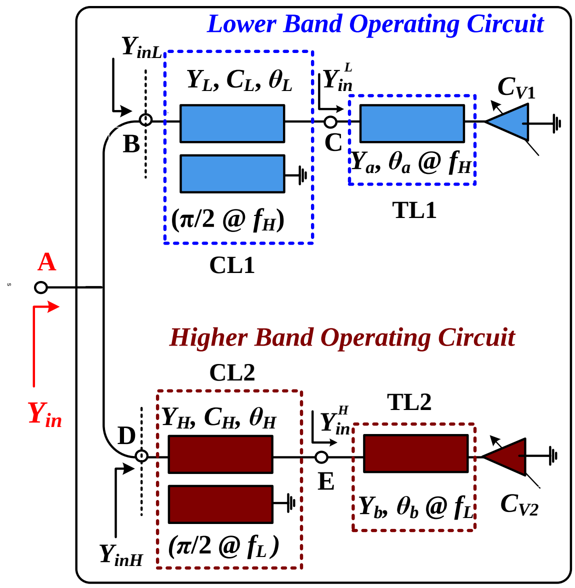

Fig. 3.1. Circuit implementation of tunable reflection load

3.2. Varactor Diode

Varactor diodes are preferred in these applications due to their low power loss caused by noise. These diodes are a type of P-N junction diode that can control the width of the depletion region when a reverse bias is applied. This control allows for adjustments in capacitance, which is crucial for managing the reactance in the reflection load of the phase shifter. By doing so, the phase characteristics can be controlled by using the bias voltage. The parasitic elements of varactor diode can lead to capacitance or inductance components that vary with frequency. This variation may cause an increase in phase deviation within the bandwidth operation. To investigate this issue, an Advanced Design System (ADS) simulation, provided by Keysight, was used. The simulation involved tweaking the parameters of the diode model to closely match the actual measurement results of the varactor diode, in this case, the SMV-1231 from Skyworks. This approach allowed for the construction of an equivalent circuit model that demonstrates similar characteristics to the real diode. The ADS simulation was used to confirm the frequency nonlinearity of the varactor diode as a function of voltage. The specific varactor diode studied, the SMV-1231, was chosen for its minimum capacitance value, which is the smallest in its product line. This characteristic enables a wider phase shift range in the reflection load due to reactance. The operating frequencies for the tests were 1.88 GHz at f_L and 2.44 GHz at f_H, and the capacitance values were measured by using a Network analyzer by varying the bis voltage from 0 V to 16V. Fig. 3.2 shows the parameter equivalent circuit model of the SMV-1231 diode. Fig. 3.3 and 3.4 shows about comparison of the simulation and measurement results for the SMV-1231 at both operating frequencies.

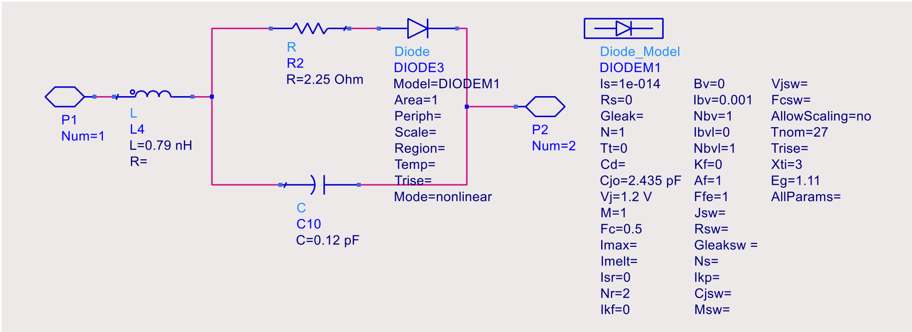

Fig. 3.2. Equivalent circuit of SMV-1231 varactor diode

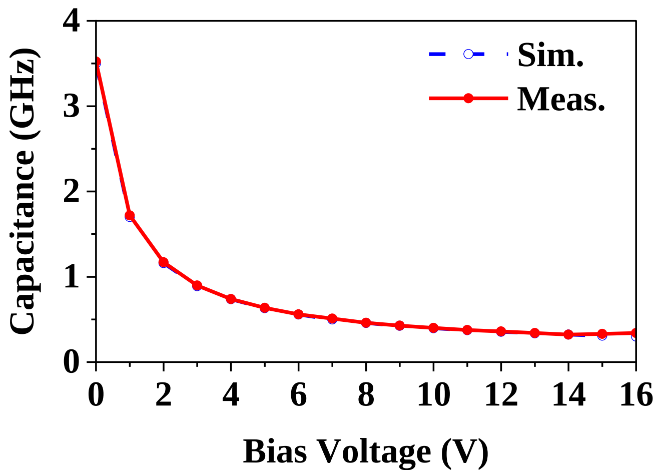

Fig. 3.3. Capacitance variation according to bias voltage at f_L

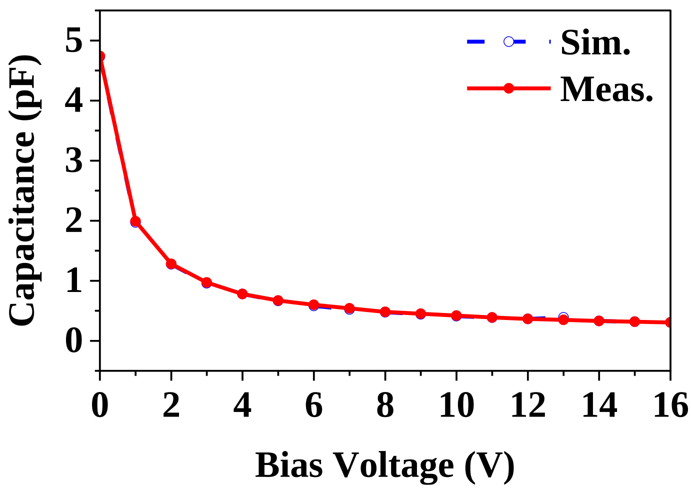

Fig. 3.4. Capacitance variation according to bias voltage at f_H

3.3. Lower Band Operation Circuit

A quarter-wavelenght of the coupled line (CL1) is used to achieve independent phase shift control at f_L. The equation 3.1 should be noted that the CL1 can provides an open condition at node B when $f = f_H$, while the CL1 acts as a capacitance at f_L is shown in Fig. 3.5(a). As the results, no phase shift occurs at f_H while tuning phase shift occurs at f_L is illustrated in Fig. 3.5(b). The input admittance at the lower band operation is given as

$$Y_{inL} = j\frac{Y_A - Y_B - 2Y_C + 2Y_D}{Y_E} \tag{3.2}$$

Where

$$Y_A = j^4\left\lfloor \left(Y_{11}^L\right)^2 - \left(Y_{12}^L\right)^2 \right\rfloor\left\lfloor \left(Y_{in}^L\right)^2 + \left(Y_{11}^L\right)^2 \right\rfloor \tag{3.3a}$$

$$Y_B = j^4\left\lfloor \left(Y_{14}^L\right)^2 + \left(Y_{24}^L\right)^2 \right\rfloor\left\lfloor \left(Y_{11}^L\right)^2 + Y_{11}^L Y_{in}^L \right\rfloor \tag{3.3b}$$

$$Y_C = j^4 Y_{in}^L Y_{12}^L \left(Y_{12}^L Y_{44}^L - Y_{42}^L Y_{14}^L\right) \tag{3.3c}$$

$$Y_D = 2j^4\left\lfloor \left(Y_{11}^L\right)^3 Y_{in}^L + Y_{44}^L Y_{12}^L Y_{42}^L Y_{14}^L \right\rfloor \tag{3.3d}$$

$$Y_E = j^4\left\lfloor \left(Y_{14}^L\right)^2 + \left(Y_{24}^L\right)^2 \right\rfloor\left\lfloor \left(Y_{11}^L\right)^2 + Y_{11}^L Y_{in}^L \right\rfloor \tag{3.3e}$$

$$Y_{11}^L = -j\frac{Y_L}{\sqrt{1-C_L^2}}\cot\theta_L \tag{3.3f}$$

$$Y_{12}^L = -j\frac{C_L Y_L}{\sqrt{1-C_L^2}}\cot\theta_L \tag{3.3g}$$

$$\theta_L = \frac{\pi f}{2f_H} \quad , \quad C_L = 10^{\left[-C_L(dB)/20\right]} \tag{3.3h}$$

$$Y_{in}^{L} = -j\frac{2\pi fY_aC_{V1} + Y_a^2\tan\dfrac{\theta_a f}{f_H}}{Y_a - 2\pi fC_{V1}\tan\dfrac{\theta_a f}{f_H}} \tag{3.3i}$$

Y_a, θ_a, and C_{V1} are characteristic admittances, electrical lengths of TL, and capacitance of varactor diode, respectively. Likewise, $Y_L = 1/Z_L$ and C_L are characteristic admittances and coupling coefficients of coupled line, which are expressed terms of even and odd-mode admittances as depicted in (3).

$$Y_{0eL} = Y_L\sqrt{\frac{1+C_L}{1-C_L}}, \qquad Y_{0oL} = Y_L\sqrt{\frac{1-C_L}{1+C_L}} \tag{3.4}$$

Using (3.1), (3.2), and (3.3), phase of the proposed DPS can be written as (4)

$$\varphi = \pi - 2\tan^{-1}\left(\frac{Y_{inL} + Y_{inH}}{Y_0}\right), \tag{3.5}$$

where $Y_0 = 1/Z_0$ is a port termination admittance.

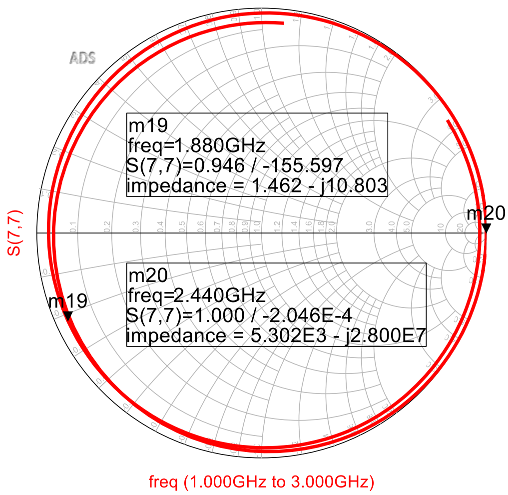

(a)

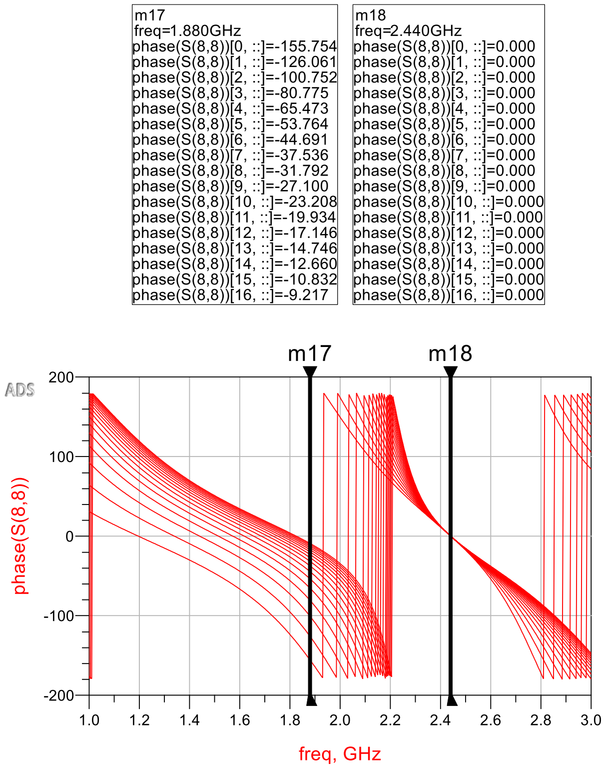

(b)

Fig. 3.5. (a) Smith chart response according to bias voltage and (b) independent tunable phase shift (ITPS) by using the coupled line

3.4. Higher Band Operation Circuit

A quarter-wavelenght of the coupled line (CL2) is used to achieve independent phase shift control at f_H. The equation 3.1 should be noted that the CL2 can provides an open condition at node D when $f = f_L$, while the CL2 acts as an inductance at f_H is shown in Fig. 3.6(a). As the results, no phase shift occurs at f_L while tuning phase shift occurs at f_H, as illustrated in Fig. 3.6(b). The input admittance at the higher band operation is given in equation (3.5).

$$Y_{inH} = j\frac{Y_F - Y_G - 2Y_H + 2Y_I}{Y_J} \tag{3.5}$$

Where

$$Y_F = j^4\left\lfloor\left(Y_{11}^H\right)^2 - \left(Y_{12}^H\right)^2\right\rfloor\left\lfloor\left(Y_{in}^H\right)^2 + \left(Y_{11}^H\right)^2\right\rfloor \tag{3.6a}$$

$$Y_G = j^4\left\lfloor\left(Y_{14}^H\right)^2 + \left(Y_{24}^H\right)^2\right\rfloor\left\lfloor\left(Y_{11}^H\right)^2 + Y_{11}^H Y_{in}^H\right\rfloor \tag{3.6b}$$

$$Y_H = j^4 Y_{in}^H Y_{12}^H\left(Y_{12}^H Y_{44}^H - Y_{42}^H Y_{14}^H\right) \tag{3.6c}$$

$$Y_I = 2j^4\left\lfloor\left(Y_{11}^H\right)^3 Y_{in}^H + Y_{44}^H Y_{12}^H Y_{42}^H Y_{14}^H\right\rfloor \tag{3.6d}$$

$$Y_J = j^4\left\lfloor\left(Y_{14}^H\right)^2 + \left(Y_{24}^H\right)^2\right\rfloor\left\lfloor\left(Y_{11}^H\right)^2 + Y_{11}^H Y_{in}^H\right\rfloor \tag{3.6e}$$

$$Y_{11}^H = -j\frac{Y_H}{\sqrt{1-C_H^2}}\cot\theta_H \tag{3.6f}$$

$$Y_{12}^H = -j\frac{C_H Y_H}{\sqrt{1-C_H^2}}\cot\theta_H \tag{3.6g}$$

$$\theta_H = \frac{\pi f}{2f_L} \quad , \quad C_H = 10^{[-C_H(dB)/20]} \tag{3.6h}$$

$$Y_{in}^H = -j\frac{2\pi f Y_b C_{V2} + Y_b^2 \tan\frac{\theta_b f}{f_L}}{Y_b - 2\pi f C_{V2}\tan\frac{\theta_b f}{f_L}} \tag{3.6i}$$

Y_b, θ_b, and C_{V2} are characteristic admittances, electrical lengths of TL, and capacitance of varactor diode, respectively. Likewise, $Y_H = 1/Z_H$ and C_H are characteristic admittances and coupling coefficients of coupled line, which are expressed terms of even and odd-mode admittances as depicted in (3.7).

$$Y_{0eL} = Y_L\sqrt{\frac{1+C_L}{1-C_L}}\ , \qquad Y_{0oL} = Y_{L,H}\sqrt{\frac{1-C_L}{1+C_L}} \tag{3.7}$$

Using (3.1), (3.2) and (3.6), phase of the proposed DPS can be written as (3.8)

$$\varphi = \pi - 2\tan^{-1}\left(\frac{Y_{inL} + Y_{inH}}{Y_0}\right), \tag{3.8}$$

where $Y_0 = 1/Z_0$ is a port termination admittance.

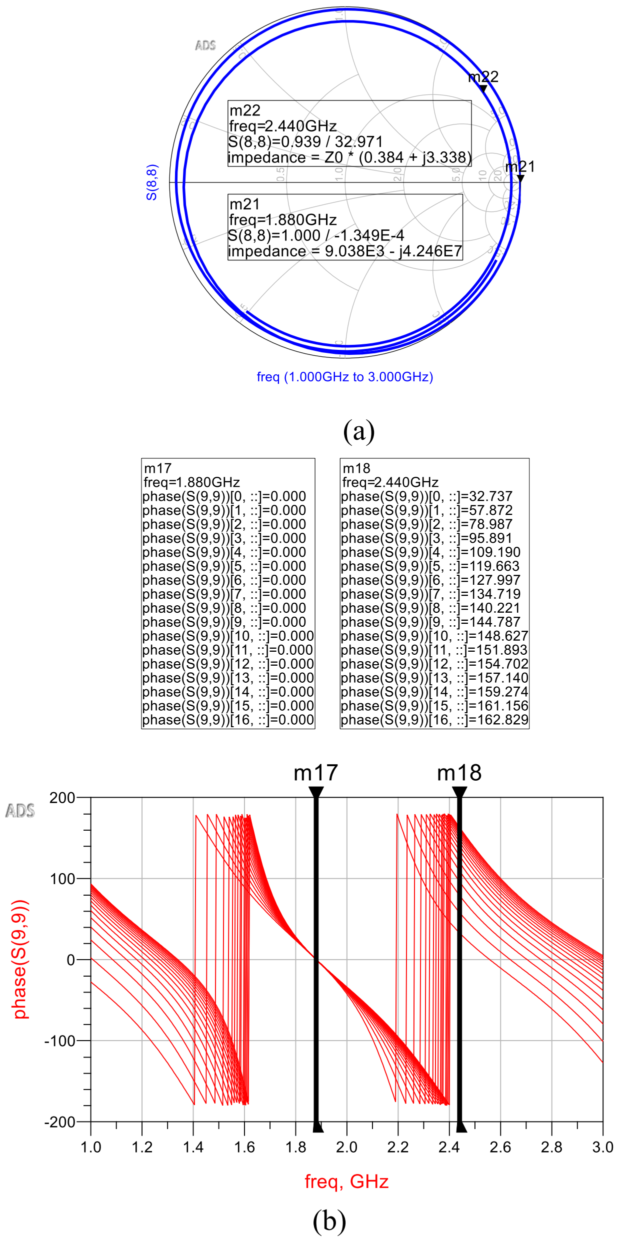

Fig. 3.6. (a) Smith chart response and (b) ITPS by using the coupled line

3.5. Flowchart of Optimization

Fig. 3.7 shows the flowchart of optimization for designing a dual-band tunable phase shifter using a particular method involving reflection load.

- ✓ Step 1: The process begins with the input of specific values including lower and higher frequencies (f_L, f_H), bandwidth (BW), number of point (NP), minimum and maximum phase shifts at both frequency limits ($\Delta\varphi_{\mathrm{min\_L}}$, $\Delta\varphi_{\mathrm{min\_H}}$, $\Delta\varphi_{\mathrm{max\_L}}$, $\Delta\varphi_{\mathrm{max\_H}}$), minimum and maximum magnitudes ($\mathrm{Mag}_{\mathrm{min}}$, $\mathrm{Mag}_{\mathrm{max}}$), voltage limits ($V_{\mathrm{min}}$, V_{max}, parasistic components of varactor diode (L_p, C_p, R_p, C_j).
- ✓ Step 2: The flowchart then splits into two paths for lower band operation and higher band operation. For lower band operation, you adjust Z_L, C_L, Z_{Ls}, and θ_{Ls}. For high band operation, you adjust Z_H, C_H, Z_{Hs}, and θ_{Hs}.
- ✓ Step 3: After these adjustments, Calculate the phase shift range ($\Delta\varphi_L$, $\Delta\varphi_H$) at the center frequency, the maximum phase deviation ($\varphi_{\mathrm{err\_L}}$, $\varphi_{\mathrm{err\_H}}$) within 300 MHz operating BW, and the maximum return loss ($\mathrm{Mag}_{\mathrm{L}}$, $\mathrm{Mag}_{\mathrm{H}}$) within 300 MHz operating BW at the both band operating frequencies by varied the bias voltage from 0 – 16 V.
- ✓ Step 4: The next step is another decision point where you compare the calculated phase shift and magnitude against reference or required values. For lower band: If $\Delta\varphi_{\mathrm{L}} > \Delta\varphi_{\mathrm{ref\_L}}$, $\varphi_{\mathrm{err\_L}} < \varphi_{\mathrm{err\_ref\_L}}$, and $\mathrm{Mag}_{\mathrm{L}} < \mathrm{Mag}_{\mathrm{ref}}$, then proceed. For high band: If $\Delta\varphi_{\mathrm{H}} > \Delta\varphi_{\mathrm{ref\_H}}$, $\varphi_{\mathrm{err\_H}} < \varphi_{\mathrm{err\_ref\_H}}$, and $\mathrm{Mag}_{\mathrm{H}} < \mathrm{Mag}_{\mathrm{ref}}$, then proceed.
- ✓ Step 5: If the conditions are met (Yes), then you check if the PDE is minimum and PSR is maximum for both low and high bands are

within acceptable limits, then go to next step.

- ✓ Step 6: The final decision point asks if the values of length, width, and gap are acceptable to fabricate. If yes, then the design is presumably finalized for fabrication. If no, then adjustments must be made.

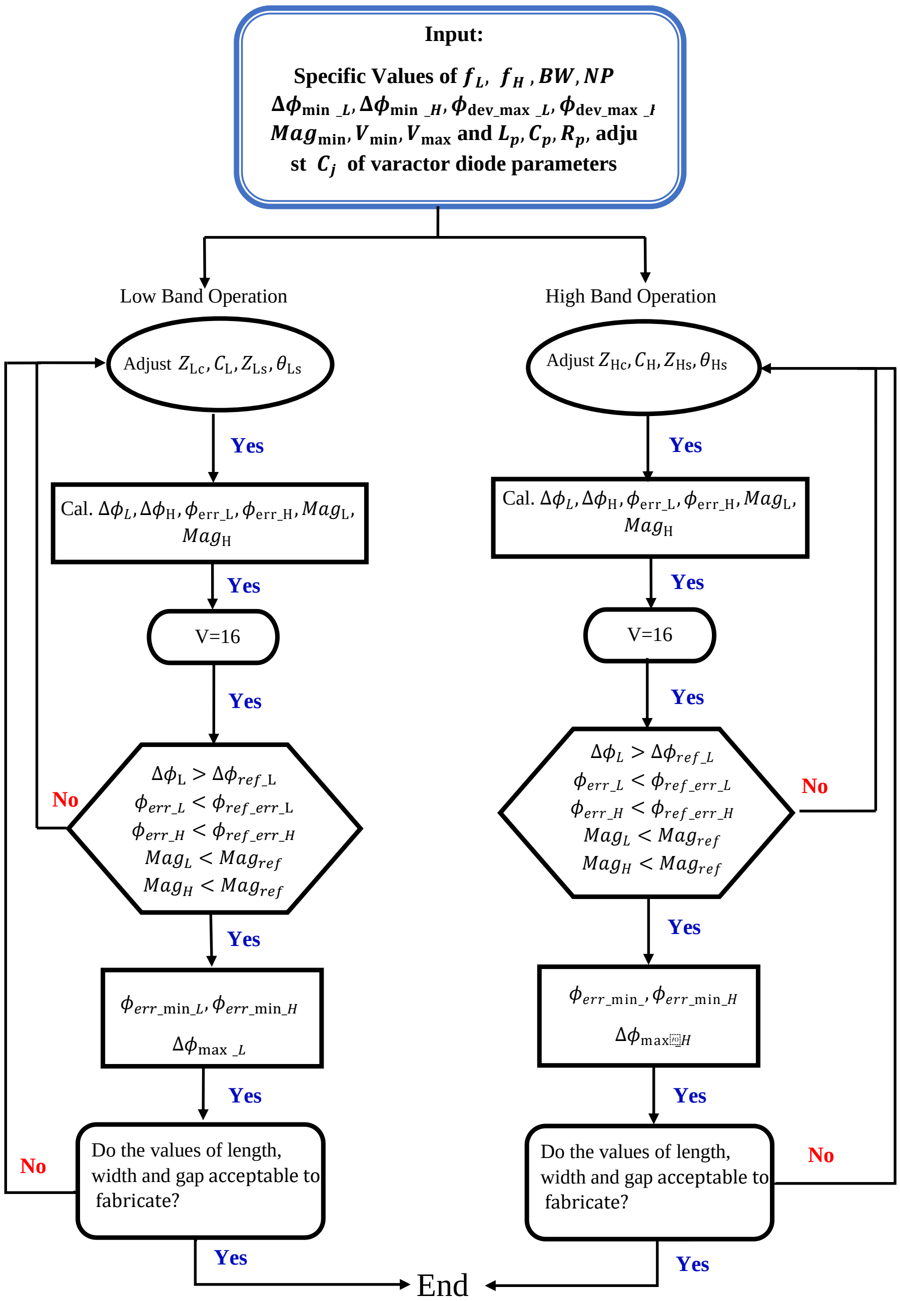

Fig. 3.7. Algorithm flowchart for designing a phase shifter

The circuit parameters of coupled lines and TLs are optimized for each operating center frequency by using MATLAB and results are shown in Tables I and II.

As seen from Table I, maximum relative PSR of 146° is achieved at lower operating center frequency f_L = 1.88 GHz with PDE of ±6.72° within bandwidth of 300 MHz, when circuit parameters are selected as $Z_L = 1/Y_L$ = 81 Ω, C_L = -8.3 dB, $Z_a = 1/Y_a$ = 120 Ω, and θ_a = 110°. Fig. 3.8 shows independent tunable phase shifter (ITPS) characteristics at lower and higher operating bands. As seen in the figure, the transmission phase shift is independently tuned at lower operating frequency band (1.73 ~ 2.03 GHz) when C_{V1} is varied and C_{V2} is fixed.

TABLE I

Calculated PSR = $\Delta\varphi_{max}$ and PDE = φ_{err} within bandwidth of 300 MHz at f_L = 1.88 GHz for different circuit parameters

<table>
<tr><th colspan="6">Varactor diode SMV-1231 with C_V: 0.3 pF to 3.5 pF</th></tr>
<tr><th>Z_L (Ω)</th><th>C_L (dB)</th><th>Z_a (Ω)</th><th>θ_a (°)</th><th>$\Delta\varphi_{max}$ (°)</th><th>φ_{err} (°)</th></tr>
<tr><td>70</td><td>-8</td><td rowspan="5">120</td><td>117</td><td>142.16</td><td>±9.76</td></tr>
<tr><td>70</td><td>-8.5</td><td>123</td><td>134.83</td><td>±8.97</td></tr>
<tr><td>80</td><td>-8</td><td>110</td><td>151.34</td><td>±8.84</td></tr>
<tr><td>81</td><td>-8.3</td><td>110</td><td>146.15</td><td>±6.72</td></tr>
<tr><td>85</td><td>-8.5</td><td>117</td><td>143.65</td><td>±9.89</td></tr>
</table>

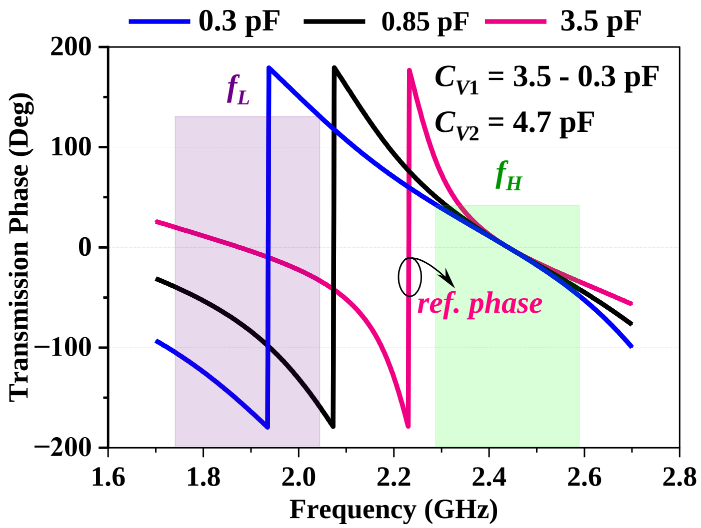

Fig. 3.8 ITPS characteristics at f_L according to C_{V1} is varied from 0.3 pF to 3.5 pF while C_{V2} is fixed at 4.7 pF.

As seen from Table II, the maximum relative PSR of 130.6° is achieved at f_H with PDE of ±8.64° within bandwidth of 300 MHz, when circuit parameters are selected as $Z_H = 1/Y_H = 70\ \Omega$, C_H = -7 dB, $Z_b = 1/Y_b = 120\ \Omega$, and $\theta_b = 123°$. Fig. 3.9 depicts the phase shift is also independently controlled at higher operating frequency band (2.29 ~ 2.59 GHz) while tuning C_{V2} and fixing C_{V1}. This independent phase shift control is achieved due to coupled lines.

TABLE II

Calculated PSR = $\Delta\varphi_{max}$ and PDE = φ_{err} within bandwidth of 300 MHz at f_H = 2.44 GHz for different circuit parameters

Varactor diode SMV-1231 with C_V: 0.3 pF to 4.7 pF					
Z_H (Ω)	C_H (dB)	Z_b (Ω)	θ_b (°)	$\Delta\varphi_{max}$ (°)	φ_{err} (°)
61	-7	110	128	135.5	±8.82
65	-7	120	125	127.14	±8.48
70	-7		123	130.6	±8.64
71	-6.9		123	133.23	±9.36
72	-7.1		123	130.62	±9.48

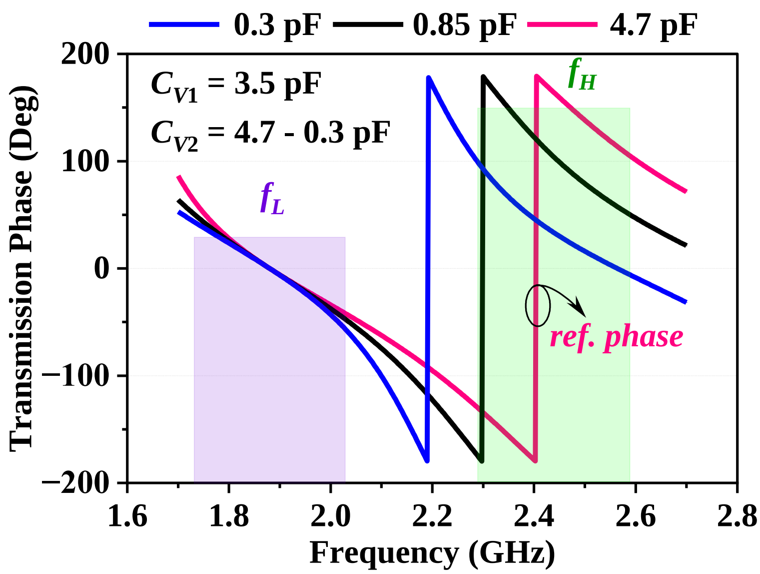

Fig. 3.9 ITPS characteristics at f_H according to C_{V1} is fixed at 3.5 pF while C_{V2} is varied from 0.3 pF to 4.7 pF.

Chapter 4 Simulation Results

The dual-band tunable phase shifter proposed in our study. The circuit parameters are selected as $Z_L = 1/Y_L = 81\ \Omega$, $C_L = -8.3$ dB, $Z_a = 1/Y_a = 120\ \Omega$, and $\theta_a = 110^\circ$ at f_L and $Z_H = 1/Y_H = 70\ \Omega$, $C_H = -7$ dB, $Z_b = 1/Y_b = 120\ \Omega$, and $\theta_b = 123^\circ$ at f_H. The performance of overall circuit was simulated by using Advanced Design System (ADS) with an ideal simulation approach. Fig. 4.1. shows the schematic of overall circuit simulation of propose dual-band tunable phase shifter. This ideal simulation was conducted in three cases: lower band operation band, higher band operation, and both band operation.

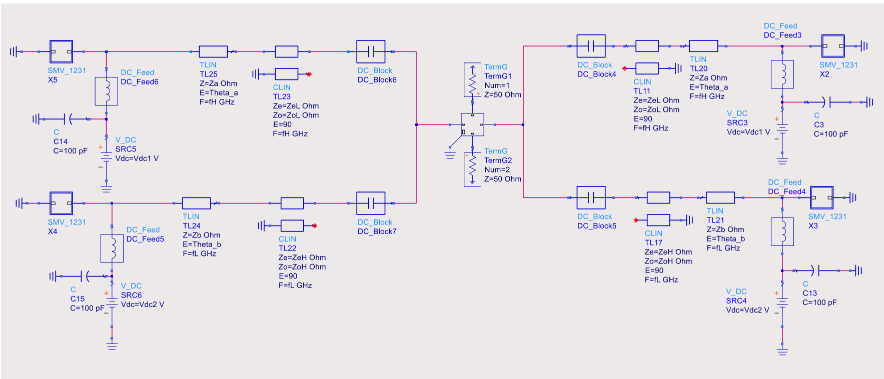

Fig. 4.1. Overall circuit simulation schematic

4.1. Lower Band Operation

The bias voltage of varactor diode operating at f_L is varied from 0 to 16 V, while the bias voltage of varactor diode operating at f_H is fixed 0 V. In this case, the maximum PSR of 146.26° is obtained at f_L, while maintaining PSR of 0° at f_H is shown in Fig. 4.2(a). Furthermore, the maximum PDE is 7.69°

at f_L and 6.5° at f_H, as shown in Figures 4.2(b) and (c). Additionally, the maximum insertion loss is depicted as 0.56 dB in Figure 4.3(a). Figure 4.3(b) illustrates the return loss according to the bias voltage of the varactor diode, with the maximum return loss is 17.48 dB at both bands.

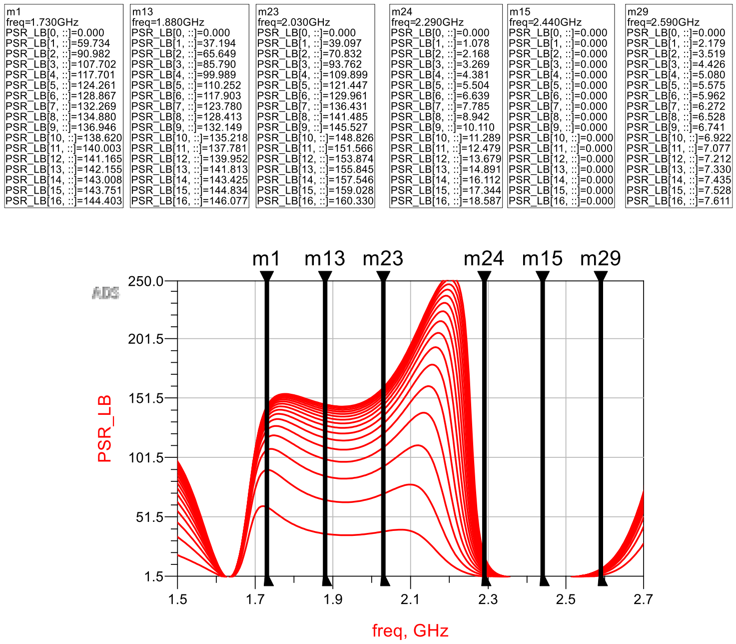

(a)

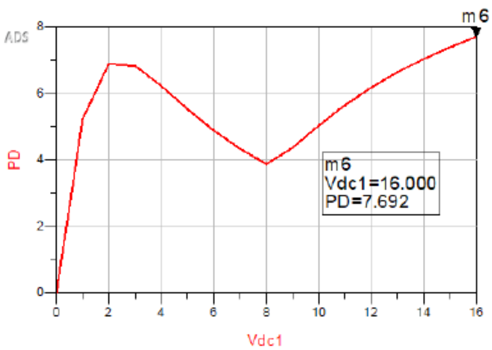

(b)

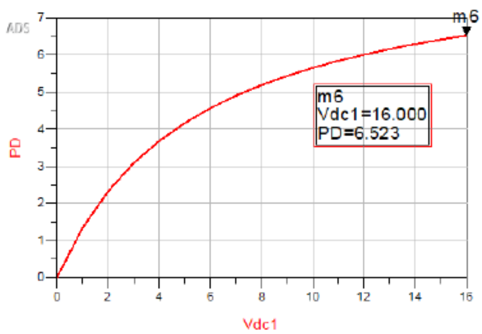

(c)

Fig. 4.2. PSR responses according to bias voltage of both bands, (b) PDE of f_L, and (c) PDE of f_H.

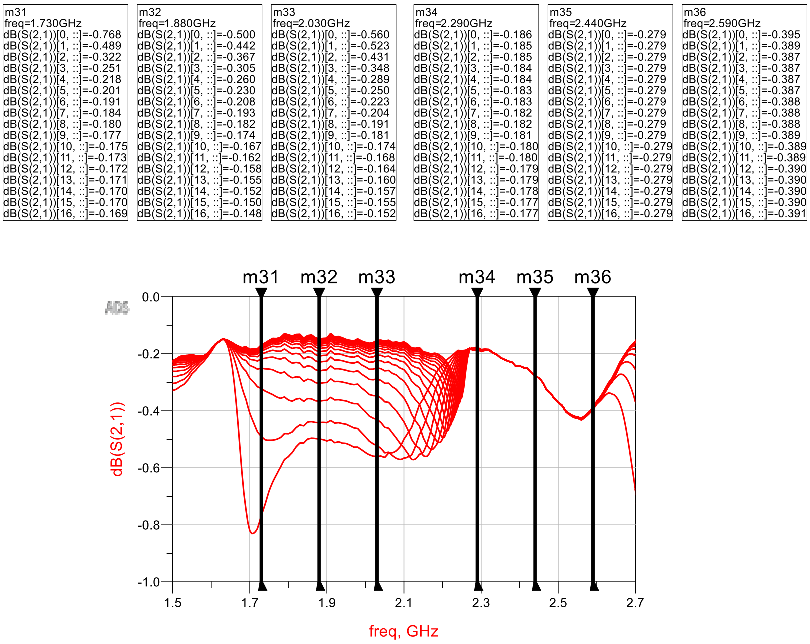

(a)

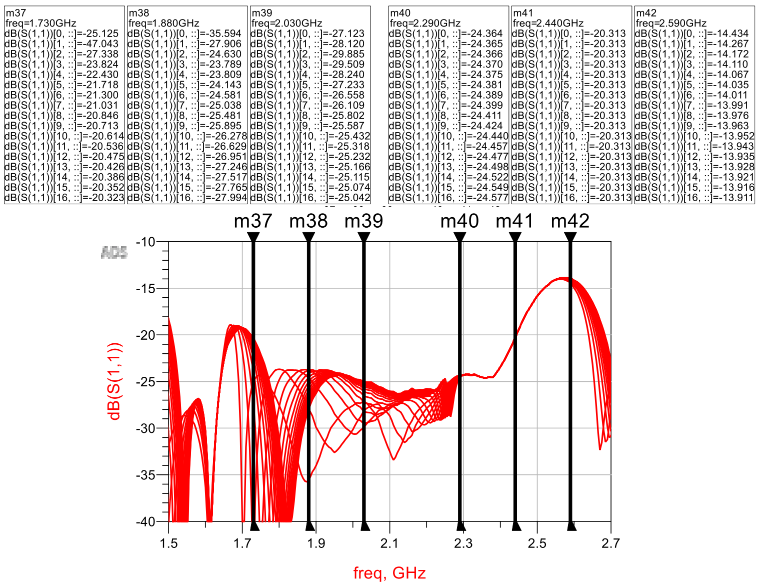

(b)

Fig. 4.3 (a) Insertion loss responses according to bias voltages of both bands, and (b) return loss responses according to bias voltages of both bands.

4.2. Higher Band Operation

Likewise to the lower band operation, the bias the bias voltage of varactor diode operating at f_L is fixed to 0 V, while the bias voltage of varactor diode operating at f_H is varied 0 to 16 V. The PSR at f_L is maintained to 0°, while the maximum PSR of 130.2° is obtained as shown in Fig. 4.4(a). Fig. 4.4(b) shows that the maximum PDE at f_L is ±8.2°, and Fig. 4.4(c) shows that the maximum PDE at f_H is ±9°. Additionally, the maximum insertion loss is 0.5 dB, as shown in Fig. 4.5(a). Fig. 4.5(b) demonstrates the return loss according to the bias voltage, with the minimum return loss is 17.48 dB at both bands.

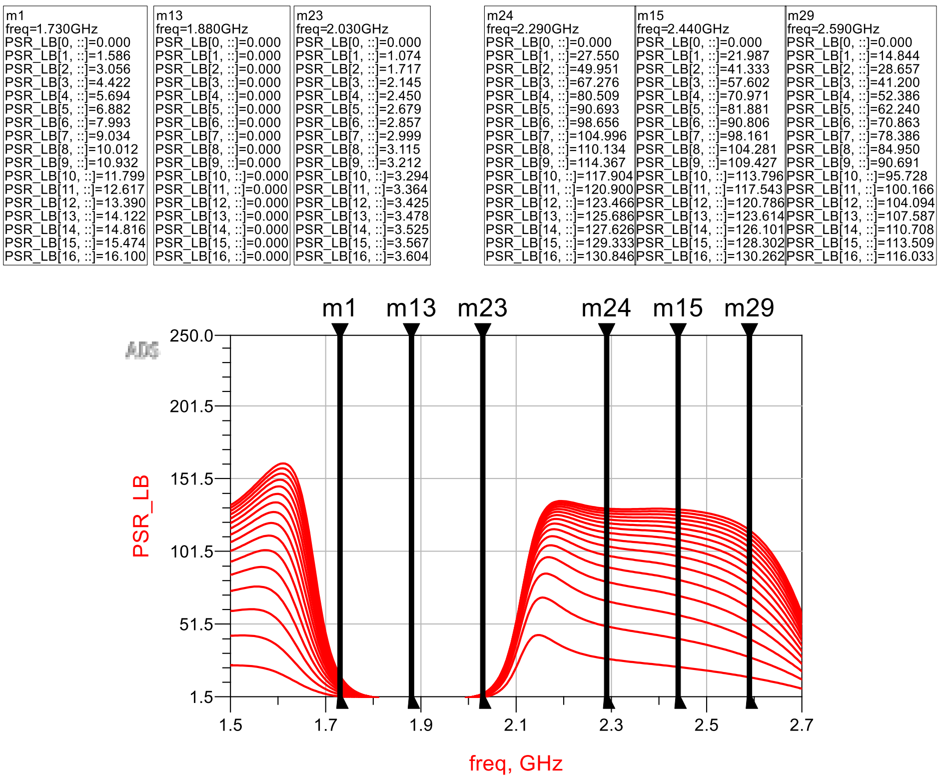

(a)

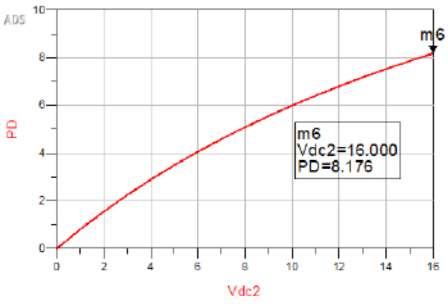

(b)

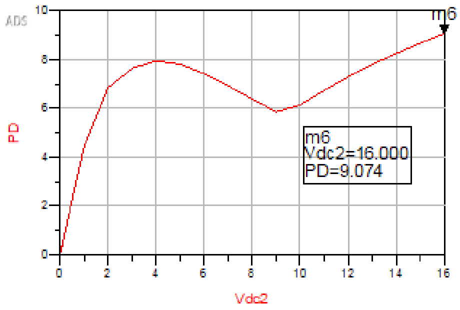

(c)

Fig. 4.4. (a) PSR responses according to bias voltage of both bands, (b) PDE of f_L, and (c) PDE of f_H.

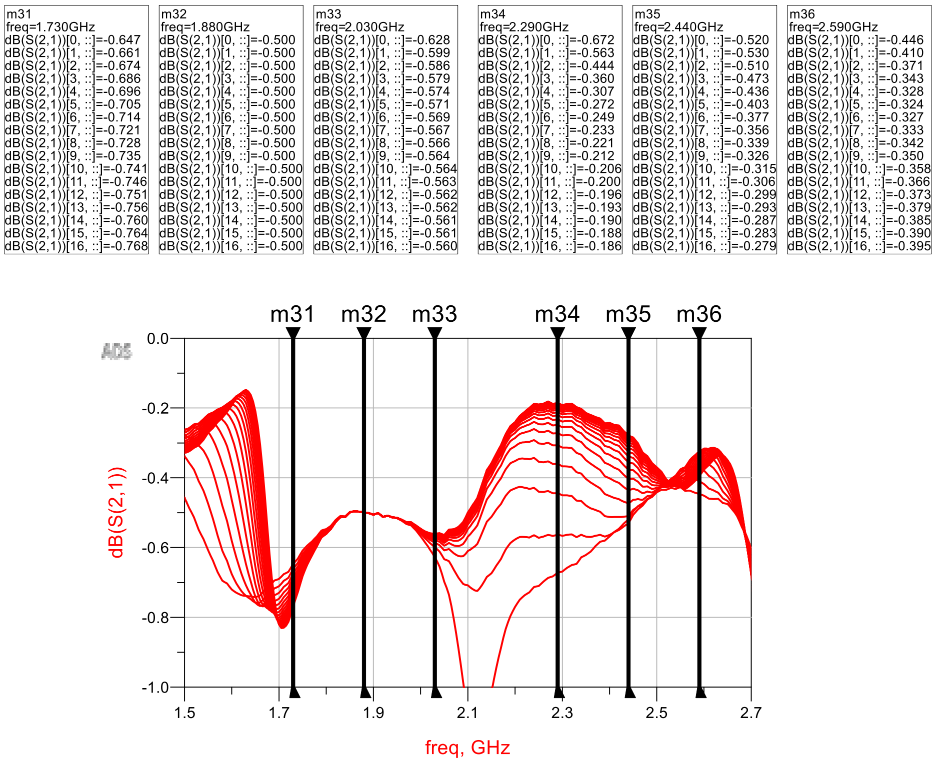

(a)

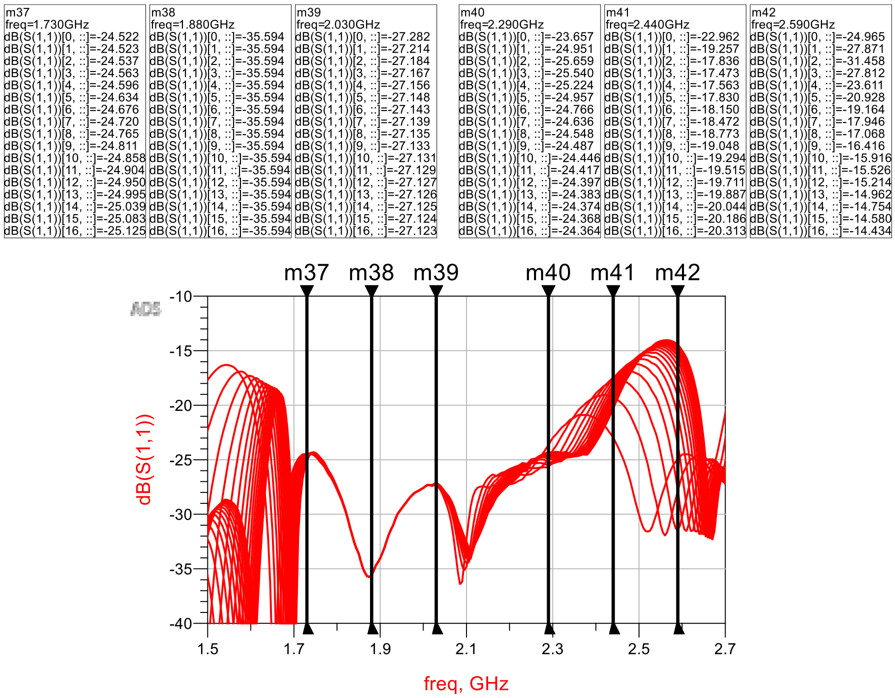

(b)

Fig. 4.5 (a) insertion loss responses according to bias voltages of both bands and (b) return loss responses according to bias voltages of both bands.

4.3. Both Bands Operation

The bias voltages of varactor diodes varying from 0 to 16 V at the both operating band. The maximum PSRs are 146° at f_L and 130.2° at f_H, as shown in Fig. 4.6(a). Furthermore, the maximum PDE within a 300 MHz range are 8.6° at f_L and 9.4° at f_H, as illustrated in Fig. 4.6(b) and 4.6(c). Additionally, the maximum insertion loss is 0.5 dB and the minimum return loss is 16.78 dB at both bands, as depicted in Fig. 4.7(a) and 4.7(b).

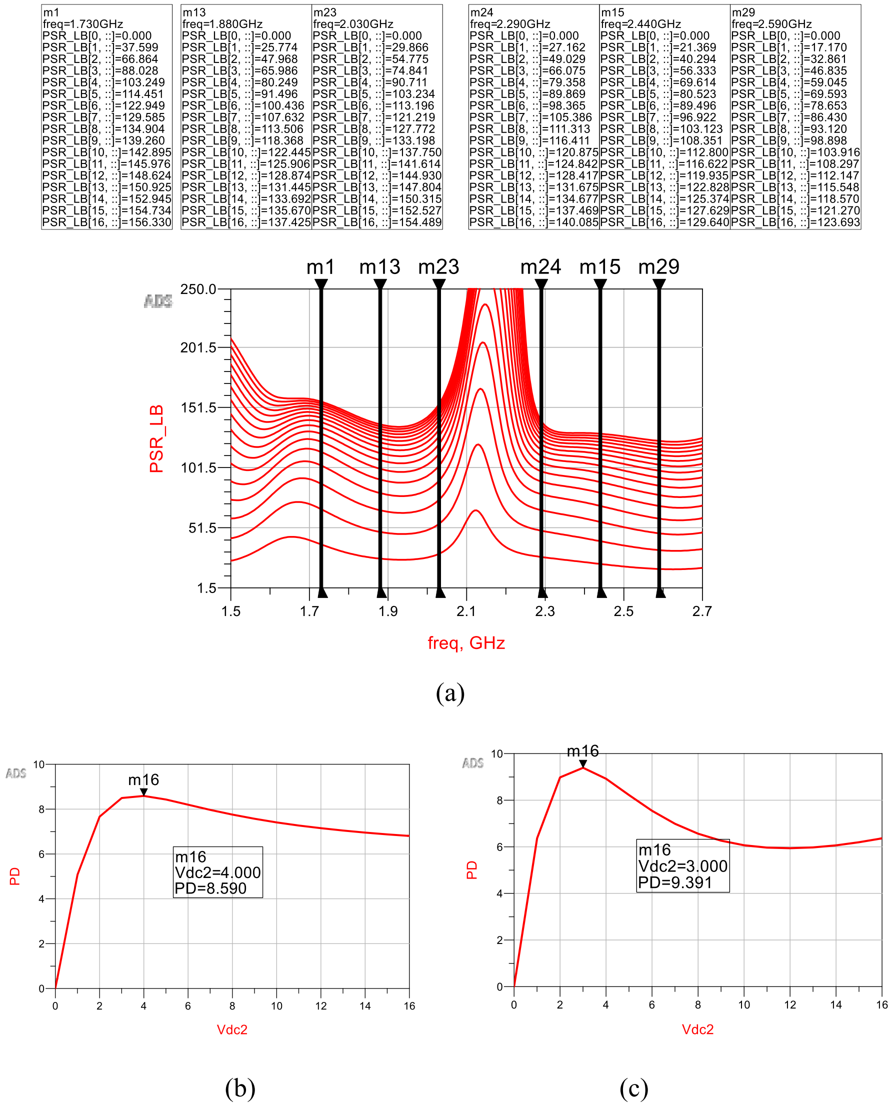

Fig. 4.6. (a) PSR responses according to bias voltage of both bands, (b) PDE of f_L, and (c) PDE of f_H.

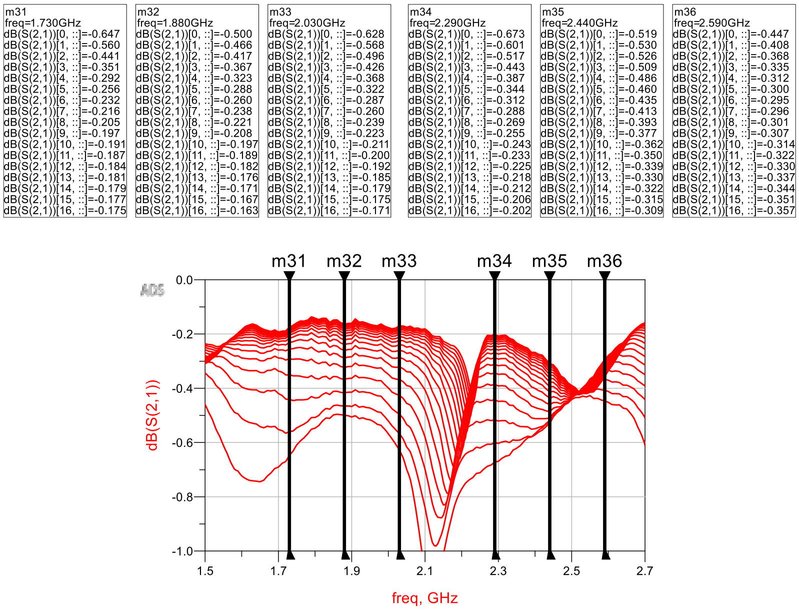

(a)

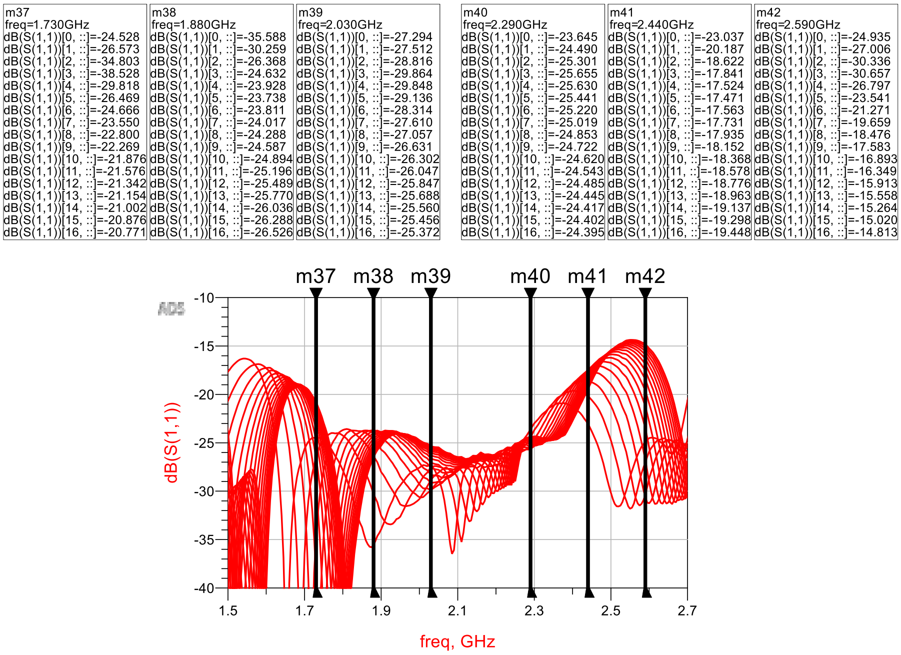

(b)

Fig. 4.7 (a) Insertion loss responses according to bias voltages of both bands and (b) return loss responses according to bias voltages of both bands.

Chapter 5 Experiment Results

For experimental validation, a prototype of tunable DPS operating at f_L = 1.88 GHz and f_H = 2.44 GHz is designed and fabricated using Taconic substrate with dielectric constant of 2.2 and thickness of 0.787 mm. Fig. 5.1 depicts the physical layout of fabricated circuit with dimensions. The photograph of fabricated circuit is shown in Fig. 5.2 and its size is 85 × 75 mm. In this work, a 3-dB hybrid coupler S03A2500N1 from ANAREN is used. The measurement results are well agreed with EM simulations. The performances of the proposed phase shifter are investigated in three cases such as lower band operation, higher band operation, and both bands operation.

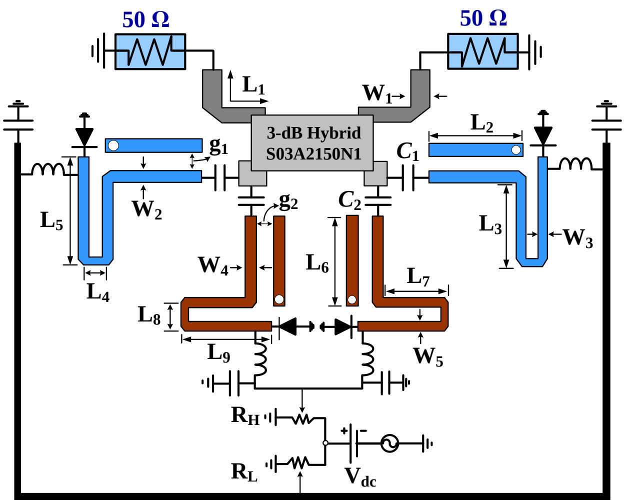

Fig. 5.1. Microstrip line implementation of proposed fully dual-band tunable phase shifter. Physical dimensions: W_1 = 2.35, L_1 = 12.8, W_2 = 0.8, L_2 = 22.6, g_1 = 0.15, W_3 = 0.5, L_3 = 15.75, L_4 = 3, L_5 = 17.55, W_4 = 0.9, L_6 = 30.7, W_5 = 0.5, L_7 = 15.75, g_2 = 0.15, L_8 = 2, L_9 = 17.55. Unit: millimeter (mm). DC block: C_1 = 56.6 pF, C_2 = 120 pF. Varactor SMV: 1231 from Skyworks Inc. Variable resistor: $R_{L, H}$ = 100 Ω .

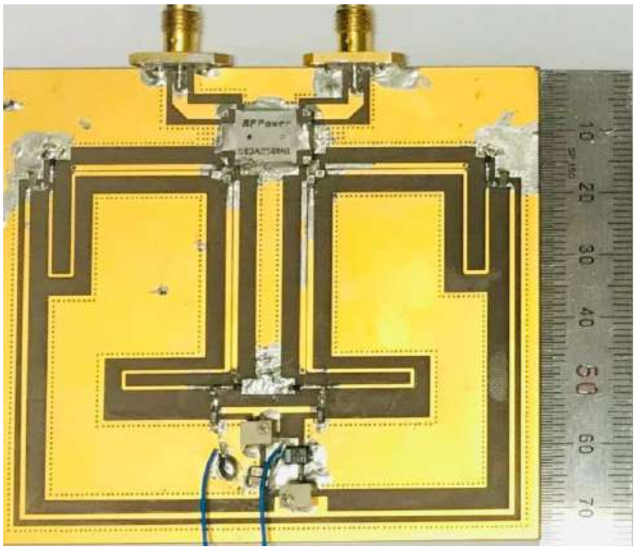

Fig. 5.2 Photograph of fabricated DPS.

5.1. Lower Band Operation

The bias voltage of varactor diode operating at lower band f_L is varied from 0 to 16 V while the bias voltage of varactor diode operating at higher band f_H is fixed 0 V. In this case, measured maximum PSR of 149.32° with PDE of ±8.25° are achieved within bandwidth of 300 MHz at f_L, while maintaining 0° phase shift at f_H, is shown in Fig. 5.3(a). Furthermore, insertion loss smaller than 1.96 dB and input/output return losses larger than 20.16 dB are measured at both operating bands is despicted in Fig. 5.3(b).

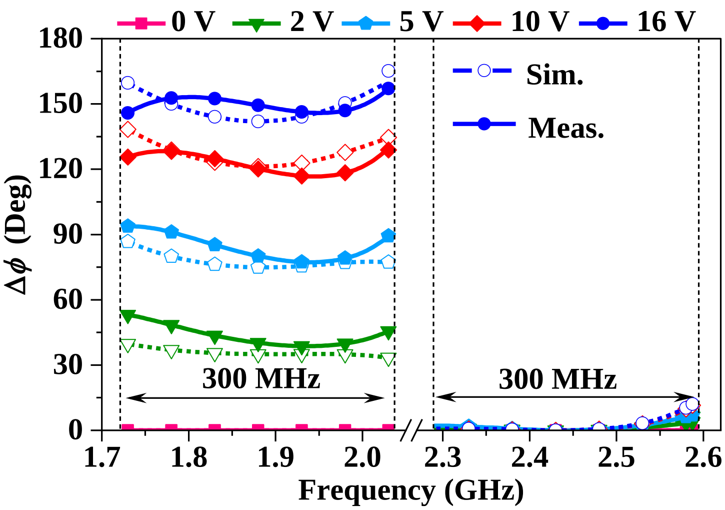

(a)

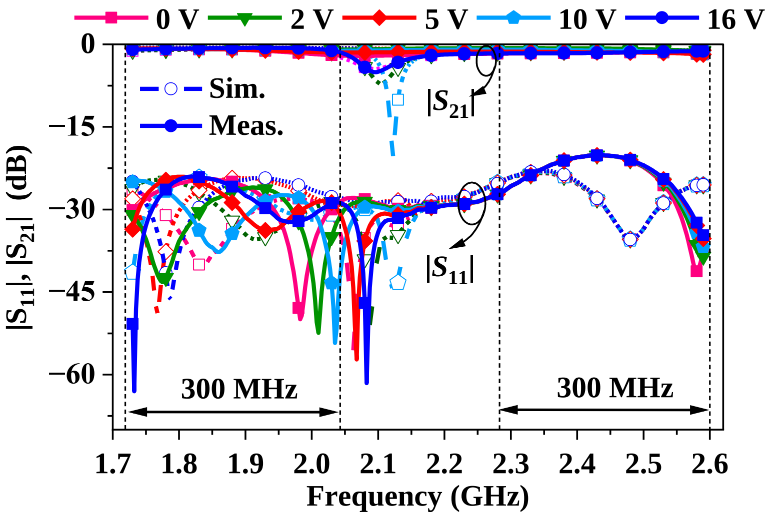

(b)

Fig. 5.3. Simulation and measurement results of the lower band operation: (a) PSR and (b) S-parameter responses.

5.2. Higher Band Operation

The bias voltage of varactor diode operating at f_L is fixed to 0 V, while the bias voltage of varactor diode operating at f_H is varied 0 to 16 V. The simulation and measured results of this case is shown in Fig. 5.4(a). From the measurement, maximum PSR of 125.14° and PDE of ±9.34° are obtained within 300 MHz bandwidth of f_H. Moreover, insertion loss smaller than 1.86 dB and input/output return losses larger than 16.14 dB are measured at both operating bands is shown in Fig. 5.4(b).

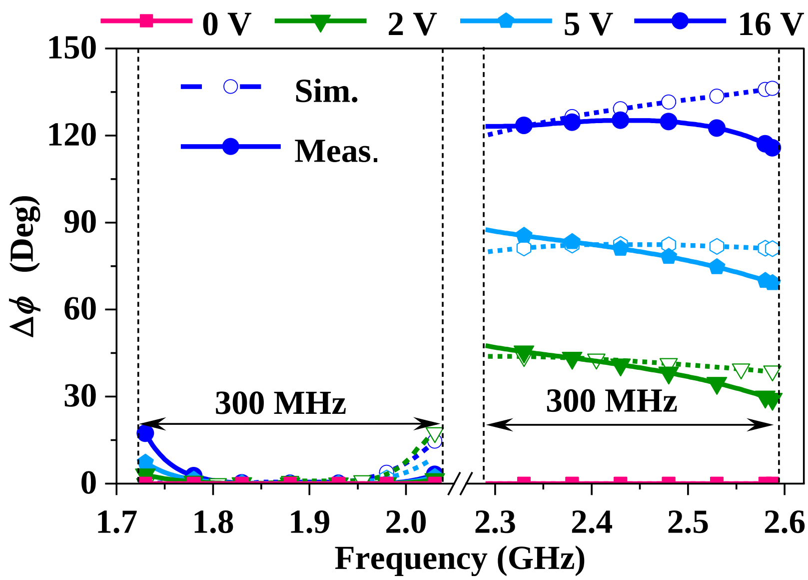

(a)

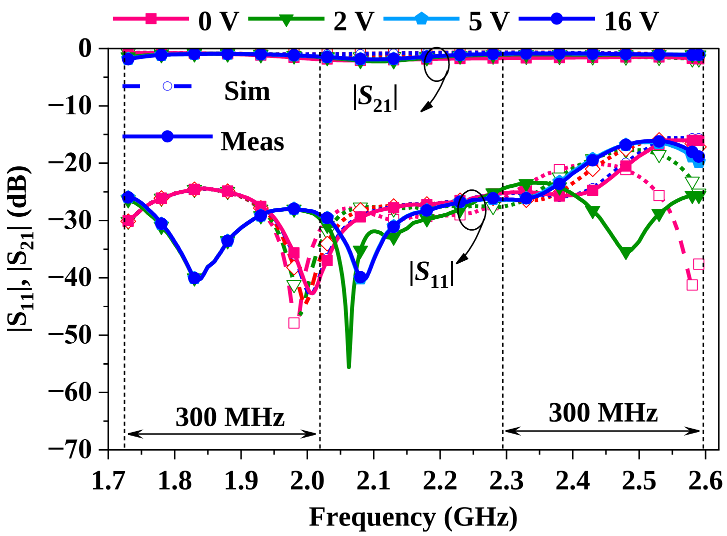

Fig. 5.5. Simulation and measurement results of higher band operation: (a) PSR and (b) *S*-parameter responses.

5.3. Both Bands Operation

Fig. 5.6 shows the simulation and measurement results of the third case where relative phase shift at both operating bands are tuned simultaneously. In this case, maximum PSR of 149.33° with PDE of ±8.45° are measured within bandwidth of 300 MHz at f_L, while maximum PSR of 125.25° with PDE of ±8.36° are measured within bandwidth of 300 MHz at f_H. The measured insertion losses vary from 1 dB to 1.96 dB at f_L and from 1.1 dB to 1.81 dB at f_H. The insertion loss can be improved by using a varactor diode with low parasitic resistance. While tuning relative PSR, the measured input/output return losses are higher than 21.1 dB at lower band operating frequency and 17.36 dB at higher band operating frequency.

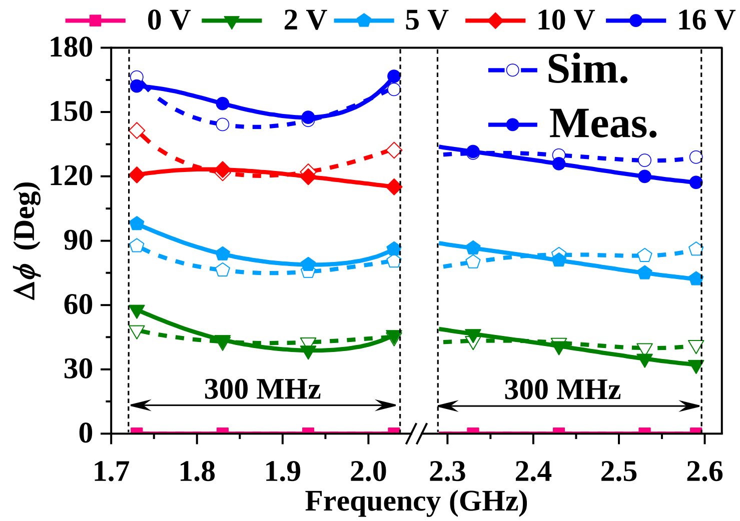

(a)

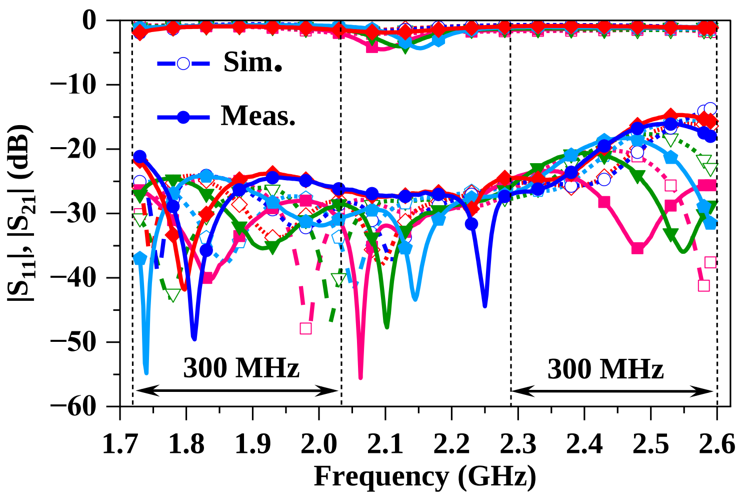

(b)

Fig. 5.5. Simulation and measurement results of the both band operation: (a) PSR and (b) *S*-parameter responses.

Table III shows the performances comparison of the proposed tunable DPS with previously reported works. In this work, the figure of merit (FoM) is defined as (5.1) by considering PSR, insertion loss (IL), return loss (RL), and bandwidth (BW).

$$\mathrm{FoM} = \frac{BW(\mathrm{GHz}) \times PSR(\mathrm{rad})}{f_0(\mathrm{GHz}) \times PDE(\mathrm{rad})} \times \frac{10^{\left(\frac{-IL(dB)}{20}\right)}}{10^{\left(\frac{-RL(dB)}{20}\right)}} \tag{5.1}$$

Most of the previously reported tunable phase shifters are designed for single-band frequency operation [4], [5], [6], [7]. In comparison to previously reported DPSs, the proposed work provides high PSR with highest FoM. Furthermore, the proposed dual-band tunable phase shifter allows independent phase shift tuning at each operating frequency as well as simultaneous phase shift tuning at both bands.

Table III

Performances comparison with state-of-the-arts

	f_0 (GHz)	BW (GHz)	FBW (%)	PSR (°)	PDE (°)	IL (dB)	RL_{min} (dB)	D/I	FOM
[10]	1.46 4.35	0.47 0.45	32.2 10.34	90* 270*	±5 ±5	<0.73 <1.28	>15 >15	Y/N	NA
[11]	5.9 16	0.2 0.4	3.39 2.5	106 108	±7 ±7	<2.8 <3.5	>10 >10	Y/Y	1.18 0.82
[12]	1.88 2.44	0.1 0.1	5.32 4	114 114	±8.4 ±5.4	<1.86 <1.89	>19.7 >16.8	Y/Y	5.60 4.83
This Work	**1.88** **2.44**	**0.3** **0.3**	**15.96** **12.30**	**149.33** **125.25**	**±8.45** **±8.36**	**<1.96** **<1.81**	**>21.1** **>17.3**	**Y/Y**	**26.08** **10.96**

FBW: Fractional Bandwidth, PSR: Relative phase shift range, PDE: phase derivation error within certain bandwidth. D: Dual-band phase shifter, I: independent control phase shift, *: differential phase shifter with fixed phase shift.

Chapter 6 Conclusion

This work presented a design of reflection-type tunable DPS that allows to control independent phase shift at each operating band as well as simultaneous tunable phase shift at both bands. This independent phase shift control is achieved due to coupled lines

For verification of the design, a dual-band phase shifter operating at two operating frequencies of 1.88 GHz and 2.44 GHz was fabricated and measured. From the measurement results, the designed dual-band phase shifter showed a PSR of 149.23° and 125.25° at the operating frequencies, respectively, and PDEs are ±8.45° and ±8.36° within 300 MHz bandwidth. Additionally, insertion losses of within 1.96 dB and 1.81 dB, and reflection losses of more than 21.1 dB and 17.3 dB were achieved in both bands.

The proposed microwave dual-band phase shifter has the advantages of low phase deviation and high reflection loss characteristics within the band, making it widely applicable in next-generation wireless communication systems. Moreover, compared to previously researched dual-band phase shifters, it is more convenient to manufacture, and its capability to handle dual-band signals with a single application offers benefits in terms of miniaturization of the product.

REFERENCES

[1] A. Ayed, I. Jaffri, A. Darwish, P. Mitran, and S. Boumaiza, " Proof-of-concept of millimeter-wave Rf beamforming transmitter architecture employing frequency-multiplier-based up-converters," *IEEE Microw. Wireless Compon. Lett*., vol. 32, no. 6, pp. 776-779, Jun. 2022.

[2] J. Kim, S. Chae, H. Jo, T. Yeo, and J. Yu, " Wideband Circularly Polarized Phased Array Antenna System for Wide Axial Ratio Scanning," *IEEE Trans. Antennas and Propag*., vol. 70, no. 2, pp. 1523-1528, Feb. 2022.

[3] S. Hong, J. Brand, J. Choi, M. Jain, J. Mehlman, S. Katti, and P. Levis, " Application of self-interference cancellation in 5G and beyond," *IEEE Commun. Mag.*, vol. 14, pp. 114-121, Feb. 2014.

[4] A. M. Abbosh, " Compact tunable reflection phase shifters using short section of coupled lines," *IEEE Trans. Microw. Theory Techn*., vol. 60, no. 8, pp. 2465–2472, Aug. 2012.

[5] W. J. Liu, S. Y. Zheng, Y. M. Pan, Y. X. Li, and Y. L. Long, " A wideband tunable reflection-type phase shifter with wide relative phase shift," *IEEE Trans. Circuits Syst. II, Exp. Briefs*, vol. 64, no.12, pp. 1442–1446, Dec. 2017.

[6] B. An, G. Chaudhary, and Y. Jeong, " Wideband tunable phase shifter with low in-band phase deviation using coupled line," *IEEE Microw. Wirel. Compon. Lett.*, vol. 28, no. 8, pp. 678–680, Aug. 2018.

[7] G. Chaudhary, B. An, and Y. Jeong, " In-band phase deviation minimization method for wideband tunable phase shifter," *Microwave Optical Techn Lett*. , vol. 61, no. 2, pp. 537-541, Feb. 2019.

[8] Y. Itoh and H. Tagagi, " A dual-band 90-degree SiGe HBT active phase shifter using band-pass and band-stop designs," *In Proc. of the European Microwave Conference (EuMC)*, pp. 10–12, 2017.

[9] Q. Dong, Y. Wu, W. Chen, Y. Yang, and W. Wang, " Single-layer dual-band bandwidth-enhanced filtering phase shifter with two different predetermined phase-shifting values," *IEEE Trans. Circuits Syst. II, Exp. Briefs.,* vol. 68, no.1, pp. 68, 236–240, Jan. 2021.

[10] Y. P. Lyu, L. Zhu, and C. H. Cheng, " Dual-band differential phase shifter using phase slope alignment on coupled resonators," *IEEE Microw. Wirel. Compon. Lett*., vol. 28, no. 12, pp. 1092–1094, Dec. 2018.

[11] Y. Xiong, X. Zeng, and J. Li, " A tunable concurrent dual-band phase shifter MMIC for beam steering applications," *IEEE Trans. Circuits Syst. II, Exp. Briefs*, vol.67, no.11, pp. 2412–2416, Nov. 2020.

[12] S. Kim, J. Jeong, G. Chaudhary, and Y. Jeong, " A reflection-type dual-band phase shifter with an independently tunable phase," *Applied Sciences,* vol. 12, no. 1, pp. 492–504, Jan. 2022.

Appendex: MATHLAB Code

Input value

f_L	f_H	BW	NP
1.88E+9	2.44E+9	300E+9	401
Z_L	Z_H	Z_a	Z_b
20:1:120	20:1:120	90:1:120	90:1:120
C_L	C_H	θ_a	θ_b
-6:0.1:-9	-6:0.1:-9	90:1:130	90:1:130
PSR_{ref}	PDE_{max}	C_{V_L}	C_{V_H}
>100	10	0.3:0.1:3.5	0.3:0.1:4.7

Main Code

```
clc; clear; close all;% close all;
Z0=50; fL=1.88E9; fH=2.44E9; BW=300E6; NP=401;
fL1=linspace(fL-BW/2,fL+BW/2,NP);
fL2=linspace(fH-BW/2,fH+BW/2,NP);
ZL=20:1:120;
Cdb_L=-8.5;
Za_L=120;
theta_a_L_deg=117;
ZH=72;
Cdb_H=-7.2;
Zb=120;
theta_a_H_deg=123;
%% Both-band Operation
Cpoint=20;
cv1=linspace(3.5E-12,0.3E-12,Cpoint);
cv2=linspace(4.7E-12,0.3E-12,Cpoint);
%% Low band operation
for b=1:length(cv1);
    PSR_Lowband(:,b)=PSR_lowband(cv1(b),cv2(1));
    PSR_Lowbandref(:,1)=PSR_lowband(cv1(1),cv2(1));
    PSR_Low(:,b)=PSR_Lowband(:,b)-PSR_Lowbandref(:,1);
    %% High band
    PSR_Highband(:,b)=PSR_highband(cv1(b),cv2(Cpoint));
PSR_Highbandref(:,1)=PSR_highband(cv1(1),cv2(Cpoint));
```

```
     PSR_High(:,b)=PSR_Highband(:,b)-
PSR_Highbandref(:,1);
     PDerr_Low(b)=(max(PSR_Low(:,b))-
min(PSR_Low(:,b)))/2;
     PDerr_High(b)=(max(PSR_High(:,b))-
min(PSR_High(:,b)))/2;
end

if PSR_Highbandref(:,1) > PSR_Highband(:,b)
    PSR_Low(:,b)=PSR_Lowbandref(:,1)-PSR_Lowband(:,b);
 else
     PSR_Low(:,b)=PSR_Lowband(:,b)-PSR_Lowbandref(:,1);
 end

%% High Band operation
for a=1:length(cv2);
    PSR_Lowband1(:,a)=PSR_lowband(cv1(Cpoint),cv2(a));

PSR_Lowbandref1(:,1)=PSR_lowband(cv1(Cpoint),cv2(1));
    PSR_Low1(:,b)=PSR_Lowband1(:,a)-
PSR_Lowbandref1(:,1);
    %%High Band
    PSR_Highband1(:,a)=PSR_highband(cv1(1),cv2(a));
    PSR_Highbandref1(:,1)=PSR_highband(cv1(1),cv2(1));

 if PSR_Highbandref1(:,1) > PSR_Highband1(:,a)
    PSR_High1(:,a)=PSR_Highbandref1(:,1)-
PSR_Highband1(:,a);
 else
    PSR_High1(:,a)=PSR_Highband1(:,a)-
PSR_Highbandref1(:,1);
 end
%    PSR_High1(:,b)=PSR_Highbandref1(:,1)-
PSR_Highband1(:,b);
     PDerr_Low1(a)=(max(abs(PSR_Low1(:,a)))-
min(abs(PSR_Low1(:,a))))/2;
```

```
    PDerr_High1(a)=(max(abs(PSR_High1(:,a)))-min(abs(PSR_High1(:,a))))/2;
end
subplot(2,2,1)
plot(fL1*1e-9,PSR_Low);
xlabel('Frequency (GHz)','FontSize',12);
ylabel('PSR [degree]','FontSize',12);
hold on;
plot(fL2*1e-9,PSR_High)
subplot(2,2,2);
plot(cv1*1e12,PDerr_Low)
xlabel('Cv','FontSize',12);
ylabel('PD [degree]','FontSize',12);

subplot(2,2,3)
plot(fL1*1e-9,PSR_Low1);
xlabel('Frequency (GHz)','FontSize',12);
ylabel('PSR [degree]','FontSize',12);
hold on;
plot(fL2*1e-9,PSR_High1)
subplot(2,2,4);
plot(cv2*1e12,PDerr_High1)
xlabel('Cv','FontSize',12);
ylabel('PD [degree]','FontSize',12);
```

Function at Lower Band Operation

```
function [PSR]=PSR_lowband(cv1,cv2)

Z0=50; fL=1.88E9; fH=2.44E9;BW=300e6;NP=401;
f=linspace(fL-BW/2,fL+BW/2,NP);
ZL=81;
Cdb_L=-8.3;
Za=120;
theta_a_L_deg=110;
ZH=70;
Cdb_H=-7;
Zb=120;
Y0=1/Z0;
theta_a_H_deg=123;

%% Low Band Operation
Z_cv_L=-j./(2*pi.*f.*cv1);
theta_L=(pi/2).*(f./fH);
theta_a_L=deg2rad(theta_a_L_deg).*(f./fH);
ZL_L=Za_L.*(Z_cv_L+j*Za_L.*tan(theta_a_L))./(Za_L+j
*Z_cv_L.*tan(theta_a_L));
YL_L=1./ZL_L;
C_L=10^(Cdb_L/20);
Yc_L=1./Zc_L;
p_L=Yc_L./sqrt((1+C_L).*(1-C_L));
m_L=-(C_L.*Yc_L)./sqrt((1+C_L).*(1-C_L));
D_L=YL_L-j*p_L.*cot(theta_L);
Y11_L=-
j*p_L.*cot(theta_L)+(p_L.*csc(theta_L)).^2./D_L;
Y12_L=-
j*m_L.*cot(theta_L)+(p_L.*m_L.*(csc(theta_L)).^2)./
D_L;
Y22_L=-
j*p_L.*cot(theta_L)+(m_L.*csc(theta_L)).^2./D_L;
Yin_LB=Y11_L-(Y12_L.^2)./(Y22_L);

S11Y_tot=(Y0-Yin_tot)./(Y0+Yin_tot);
```

```
mag_tot=abs(S11Y_tot);
PSR=rad2deg(unwrap(angle(S11Y_tot)));

%% High-band operation
Z_cv_H=-j./(2*pi.*f.*cv2);
theta_H=(pi/2).*(f./fL);
theta_a_H=deg2rad(theta_a_H_deg).*(f./fL);
ZL_H=Za_H.*(Z_cv_H+j*Za_H.*tan(theta_a_H))./(Za_H+j
*Z_cv_H.*tan(theta_a_H));
YL_H=1./ZL_H;
Yc_H=1./Zc_H;
C_H=10^(Cdb_H/20);
p_H=Yc_H./sqrt((1+C_H).*(1-C_H));
m_H=-C_H.*Yc_H./sqrt((1+C_H).*(1-C_H));
D_H=YL_H-j*p_H.*cot(theta_H);
Y11_H=-
j*p_H.*cot(theta_H)+(p_H.*csc(theta_H)).^2./D_H;
Y12_H=-
j*m_H.*cot(theta_H)+(p_H.*m_H.*(csc(theta_H)).^2)./
D_H;
Y22_H=-
j*p_H.*cot(theta_H)+(m_H.*csc(theta_H)).^2./D_H;
Yin_HB=Y11_H-(Y12_H.^2)./(Y22_H);

%% Combine both-band operation
Yin_tot=Yin_LB+Yin_HB;
S11Y_tot=(Y0-Yin_tot)./(Y0+Yin_tot);
mag_tot=abs(S11Y_tot);
PSR=rad2deg(unwrap(angle(S11Y_tot)));
```

Function at Higher Band Operation

```
function [PSR]=PSR_highband(cv1,cv2)

Z0=50; fL=1.88E9; fH=2.44E9;BW=300e6;NP=401;
f=linspace(fH-BW/2,fH+BW/2,NP);
ZL=81;
Cdb_L=-8.3;
Za=120;
theta_a_L_deg=110;
ZH=70;
Cdb_H=-7;
Zb=120;
Y0=1/Z0;
theta_a_H_deg=123;

%% Low Band Operation
Z_cv_L=-j./(2*pi.*f.*cv1);
theta_L=(pi/2).*(f./fH);
theta_a_L=deg2rad(theta_a_L_deg).*(f./fH);
ZL_L=Za_L.*(Z_cv_L+j*Za_L.*tan(theta_a_L))./(Za_L+j*Z_cv
_L.*tan(theta_a_L));
YL_L=1./ZL_L;
C_L=10^(Cdb_L/20);
Yc_L=1./Zc_L;
p_L=Yc_L./sqrt((1+C_L).*(1-C_L));
m_L=-(C_L.*Yc_L)./sqrt((1+C_L).*(1-C_L));
D_L=YL_L-j*p_L.*cot(theta_L);
Y11_L=-j*p_L.*cot(theta_L)+(p_L.*csc(theta_L)).^2./D_L;
Y12_L=-
j*m_L.*cot(theta_L)+(p_L.*m_L.*(csc(theta_L)).^2)./D_L;
Y22_L=-j*p_L.*cot(theta_L)+(m_L.*csc(theta_L)).^2./D_L;
Yin_LB=Y11_L-(Y12_L.^2)./(Y22_L);


%% High-band operation
Z_cv_H=-j./(2*pi.*f.*cv2);
theta_H=(pi/2).*(f./fL);
```

```
theta_a_H=deg2rad(theta_a_H_deg).*(f./fL);
ZL_H=Za_H.*(Z_cv_H+j*Za_H.*tan(theta_a_H))./(Za_H+j*Z_cv
_H.*tan(theta_a_H));
YL_H=1./ZL_H;
Yc_H=1./Zc_H;
C_H=10^(Cdb_H/20);
p_H=Yc_H./sqrt((1+C_H).*(1-C_H));
m_H=-C_H.*Yc_H./sqrt((1+C_H).*(1-C_H));
D_H=YL_H-j*p_H.*cot(theta_H);

Y11_H=-j*p_H.*cot(theta_H)+(p_H.*csc(theta_H)).^2./D_H;
Y12_H=-
j*m_H.*cot(theta_H)+(p_H.*m_H.*(csc(theta_H)).^2)./D_H;
Y22_H=-j*p_H.*cot(theta_H)+(m_H.*csc(theta_H)).^2./D_H;
Yin_HB=Y11_H-(Y12_H.^2)./(Y22_H);

%% Combine both-band operation
Yin_tot=Yin_LB+Yin_HB;
S11Y_tot=(Y0-Yin_tot)./(Y0+Yin_tot);
mag_tot=abs(S11Y_tot);
PSR=rad2deg(unwrap(angle(S11Y_tot)));
```